Research
A SCIENCE PARTNER JOURNAL

RESEARCH ARTICLE

Graded Heterojunction Improves Wide-Bandgap Perovskite for Highly Efficient 4-Terminal Perovskite/Silicon Tandem Solar Cells

Wenming Chai[1†], Lindong Li[1†], Weidong Zhu[1,2*], Dazheng Chen[1,2], Long Zhou[1,2], He Xi[1], Jincheng Zhang[1], Chunfu Zhang[1,2*], and Yue Hao[1]

[1]State Key Discipline Laboratory of Wide Band Gap Semiconductor Technology & Shaanxi Joint Key Laboratory of Graphene, School of Microelectronics, Xidian University, Xi'an, Shaanxi 710071, China. [2]Xi'an Baoxin Solar Technology Co., Ltd., Xi'an, 710071, China.

*Address correspondence to: wdzhu@xidian.edu.cn (W.Z.); cfzhang@xidian.edu.cn (C.Z.)
†These authors contributed equally to this work.

Citation: Chai W, Li L, Zhu W, Chen D, Zhou L, Xi H, Zhang J, Zhang C, Hao Y. Graded Heterojunction Improves Wide-Bandgap Perovskite for Highly Efficient 4-Terminal Perovskite/Silicon Tandem Solar Cells. *Research* 2023;6:Article 0196. https://doi.org/10.34133/research.0196

Submitted 28 April 2023
Accepted 25 June 2023
Published 17 July 2023

Copyright © 2023 Wenming Chai et al. Exclusive licensee Science and Technology Review Publishing House. No claim to original U.S. Government Works. Distributed under a Creative Commons Attribution License 4.0 (CC BY 4.0).

Wide-bandgap (WBG) perovskite solar cells (PSCs) are essential for highly efficient and stable silicon/perovskite tandem solar cells. In this study, we adopted a synthetic strategy with lead thiocyanate ($Pb(SCN)_2$) additive and methylammonium chloride (MACl) posttreatment to enhance the crystallinity and improve the interface of WBG perovskite films with a bandgap of 1.68 eV. The excessive PbI_2 was formed at grain boundaries and converted into $MAPbI_{3-x}Cl_x$ perovskites, which are utilized to form the graded heterojunction (GHJ) and compressive strain. This is beneficial for passivating nonradiative recombination defects, suppressing halide phase segregation, and facilitating carrier extraction. Subsequently, the device with GHJ delivered a champion efficiency of 20.30% and superior stability in ambient air and under 85 °C. Finally, we achieved a recorded efficiency of 30.91% for 4-terminal WBG perovskite/TOPCon tandem silicon solar cells. Our findings demonstrate a promising approach for fabricating efficient and stable WBG PSCs through the formation of GHJ.

Introduction

Perovskite solar cells (PSCs) have attracted substantial attention due to their outstanding properties and potential as the next-generation photovoltaic technology [1–6]. The single-junction PSCs have already achieved a certified power conversion efficiency (PCE) of 26%, which is close to the efficiency of single-crystalline silicon solar cells [7,8]. To surpass the Shockley–Queisser limit, researchers have proposed using tandem devices by connecting multiple single cells in series [9–12]. One of the most promising approaches for tandem solar cells is to use a wide-bandgap (WBG) perovskite (approximately 1.7 eV) as the top cell and a silicon bottom cell [12–15]. Therefore, high-quality WBG film is crucial for achieving efficient tandem devices.

WBG perovskites are typically produced by replacing iodide with bromide or substituting monovalent cations with cesium [16,17]. However, under illumination, this can lead to phase segregation and large open-circuit voltage (V_{OC}) deficits, which can negatively impact device performance [14,18–21]. Researchers have developed several strategies to improve WBG perovskite films and enhance device efficiency. One of these approaches involves using organic molecules to modify the interface and improve energy level alignment [22,23]. Huang et al. [24] employed indene-C60 bisadduct-trans3 (ICBA) to reduce energy disorder in WBG PSCs and obtained a recorded PCE of 18.5%. Liu et al. [25] designed a self-assembled monolayer to minimize energy losses at the interface and achieved a high V_{OC} of 1.25 V in WBG PSCs. However, organic molecules have the disadvantages of inferior stability and high cost. Additionally, the long-chain or aromatic molecules were used to form low-dimensional perovskite and suppress ion migration [16,26–28]. For example, Liu et al. employed surface reconstruction and bifacial passivation method to minimize nonradiative recombination in 1.65-eV bandgap PSCs by posttreatment with methylammonium thiocyanate and phenethylammonium iodide [14]. A thin Ruddlesden–Popper perovskite layer was formed to create a hybrid 2-dimensional (2D)/3-dimensional heterostructure in WBG PSCs (1.72 eV) with the *n*-butylammonium bromide (BABr), which exhibited a remarkable PCE of 19.4% and V_{OC} of 1.31 V [29]. Yu et al. [30] introduced a 2D additive of 4-fluorophenylethylammonium iodide to simultaneously improve perovskite crystallization and passivate defects. Although these 2D additives can improve V_{OC} and stability, the carrier transport is limited because of their electrically insulating nature [31,32].

It is common that lead thiocyanate ($Pb(SCN)_2$) was applied to improve crystallization and increase grain size to 1 μm in WBG perovskite films [33]. Unfortunately, the $Pb(SCN)_2$ can induce excess PbI_2 formation and damage device performance. Many researchers employed the solvent annealing process to avoid excess PbI_2 formation and form a perovskite homojunction [4,34,35]. Furthermore, the incorporation of

phenethylammonium iodide and $Pb(SCN)_2$ could effectively enhance the crystallinity of WBG perovskite films and inhibit the excess PbI_2 [36,37]. However, the 2D perovskite simultaneously was formed on the surface and affected charge transport. Therefore, it is challenging to simultaneously suppress the ion migration and improve carrier transport.

In this study, we have developed a surface in-situ restructure strategy to construct the graded heterojunction (GHJ) by introducing a conventional additive of $Pb(SCN)_2$ and methylammonium chloride (MACl) posttreatment. The $Pb(SCN)_2$ additive was utilized to enhance crystallization and form excessive PbI_2 at grain boundaries. Subsequently, MACl posttreatment was employed to react with excessive PbI_2 and transformed into $MAPbI_{3-x}Cl_x$ perovskite, which can form GHJ and compressive stress on the surface. These benefits improve energy level alignment and suppression of ions migration, resulting in low nonradiative recombination and enhanced carrier transport. Consequently, the optimal WBG PSC achieved an impressive PCE of 20.30% and outstanding stability in ambient air and at an elevated temperature. Furthermore, we achieved a recorded efficiency of 30.91% in 4-terminal (4-T) perovskite/silicon tandem devices. The study demonstrates the effect of GHJs on promoting the performance and stability of WBG PSCs.

Results

The $FA_{0.65}MA_{0.20}Cs_{0.15}Pb(I_{0.8}Br_{0.2})_3$ has an optimal bandgap of 1.68 eV for perovskite/silicon tandem devices to achieve high efficiency [14,26]. The low ratio of bromide and iodide is conducive to suppressing halide phase segregation [38]. However, with the increased content of cesium, the crystal quality of perovskite films and V_{OC} of WBG PSCs decreases gradually. Thus, we employed the $Pb(SCN)_2$ additive to enhance crystallization and MACl posttreatment to remove excessive PbI_2. As shown in Fig. 1A, all x-ray photoelectron spectroscopy (XPS) spectra were calibrated using 284.8 eV of C 1s as a reference point [20]. S 2p was not detected in any of the samples (Fig. S1), indicating that SCN^- was volatilized during the annealing process. The perovskite film with both $Pb(SCN)_2$ additive and MACl posttreatment shows the presence of Cl 2p (Fig. 1B), suggesting that the chlorine ions are diffused into the crystal lattice. Furthermore, the Pb 4f and I 3d peaks show no shift in the sample with $Pb(SCN)_2$ additive, while those with MACl posttreatment exhibited a shift toward higher binding energy (Fig. 1C and D), indicating changes in the local chemical states of the sample. As illustrated in Fig. 1E, the volatilization of SCN^- ions during annealing resulted in the formation of excessive PbI_2 in perovskite films with $Pb(SCN)_2$ additive. The excessive PbI_2 then reacted with MACl during posttreatment, forming $MAPbI_{3-x}Cl_x$ perovskite and WBG/$MAPbI_{3-x}Cl_x$ GHJ on the surface. The depth analysis was employed to confirm the distribution of GHJ after Ar^+ etching at different times. As shown in Fig. S2, the chloride ions can be detected after etching 30 s, whereas they disappeared after etching 60 s. Moreover, the Pb 4f peak shifted to the higher binding energy after etching, whereas the I 3d peak shifted to a lower value. This indicates that the GHJ is formed near the upper surface.

Figure 2A to C provides scanning electron microscope (SEM) images, in which the grain is visibly larger after introducing $Pb(SCN)_2$ additive, indicating improved crystallinity and a reduction in defects. The statistical analysis of grain size, as presented in Fig. S3, indicates that the average value increases from 198.8 to 747.4 nm after adding $Pb(SCN)_2$. The excessive PbI_2 is formed at grain boundaries, which can be removed by MACl posttreatment [39,40]. However, MACl posttreatment has a negligible effect on crystallinity. As shown in Fig. S4, residual PbI_2 is observed in the samples containing $Pb(SCN)_2$ additive, even after washing with isopropyl alcohol (IPA), suggesting that the excessive PbI_2 has indeed reacted with MACl. As the atomic force microscope images are presented in Fig. 2E

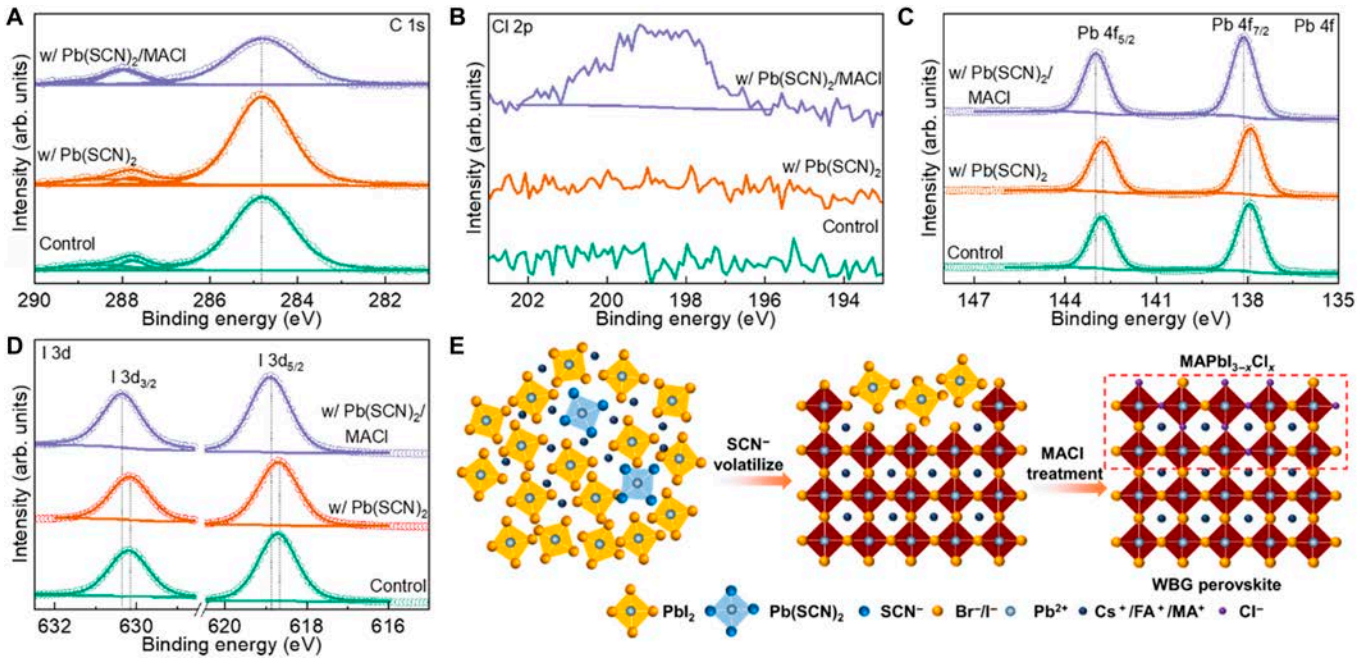


Fig. 1. XPS core-level spectra for (A) C 1s, (B) Cl 2p, (C) Pb 4f, and (D) I 3d of control WBG perovskite film, the samples with $Pb(SCN)_2$ additive, and MACl posttreatment. (E) Schematic of component variation in the WBG perovskite film with $Pb(SCN)_2$ additive and MACl posttreatment.

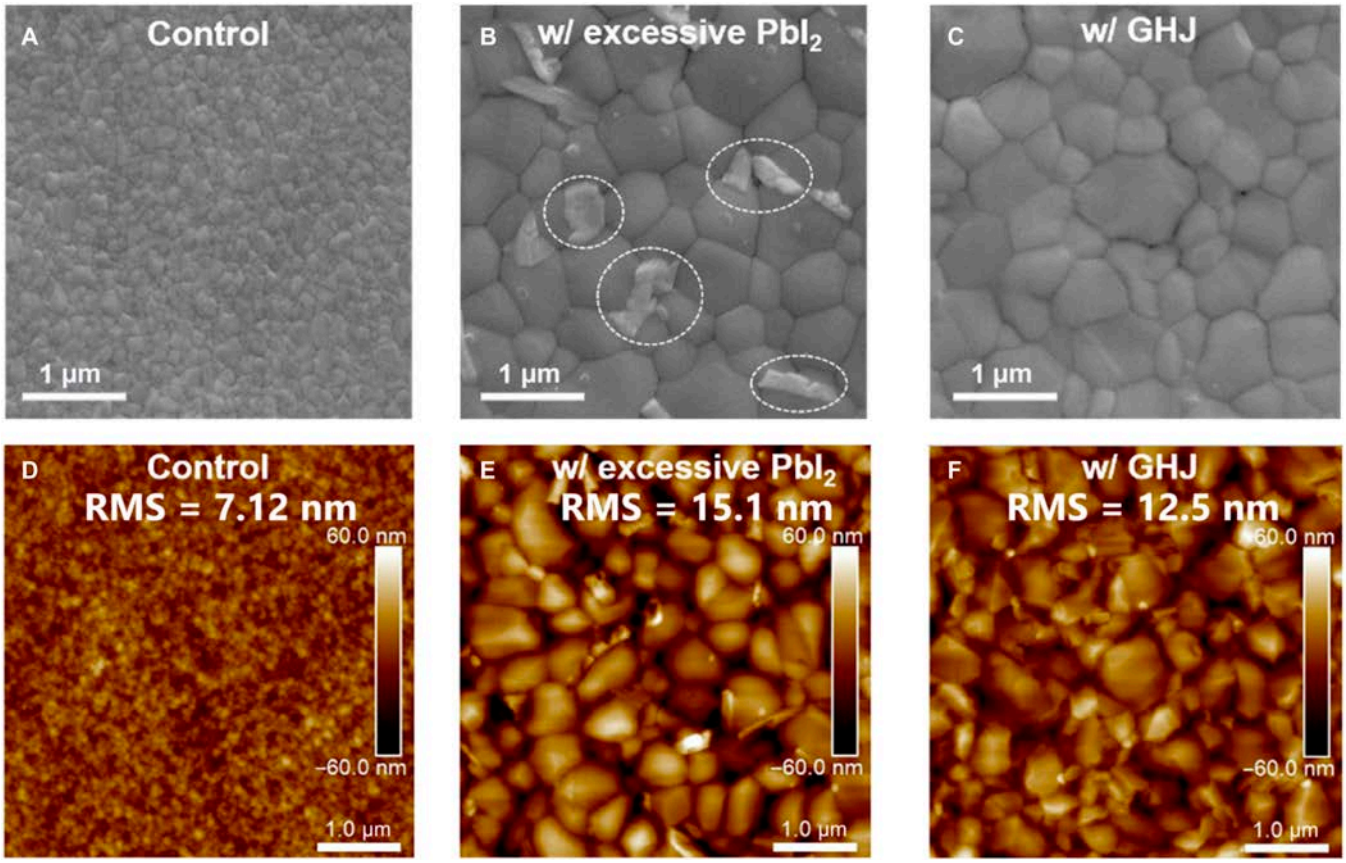


Fig. 2. SEM images of (A) the control sample, and WBG films with (B) excessive PbI_2 and (C) GHJ, respectively. AFM images of (D) the control sample, and WBG films with (E) excessive PbI_2 and (F) GHJ, respectively.

to G, the $Pb(SCN)_2$ additive increased surface roughness owing to coarsened grains and excessive PbI_2. However, MACl posttreatment resulted in a reduction in surface roughness, indicating that excessive PbI_2 was removed. Therefore, the synergistic of $Pb(SCN)_2$ additive and MACl posttreatment can improve the crystallization of WBG films.

X-ray diffraction (XRD) was employed to perform the crystalline structure of the WBG films with $Pb(SCN)_2$ additive and subsequent treatment with MACl [41]. Two distinctive diffraction peaks are seen at 14.06° and 28.19°, which correspond to the (100) and (200) crystal planes of the α-phase, as presented in Fig. 3A [36,42]. Additionally, a new peak appears at 12.38° corresponding to PbI_2, indicating that $Pb(SCN)_2$ additive formed excessive PbI_2 on the surface [43]. The intensity of (100) and (200) planes is enhanced in the samples with the $Pb(SCN)_2$ additive and MACl posttreatment [44]. Meantime, the diffraction peaks shifted to a higher degree (Fig. S5), resulting from the excessive PbI_2 and smaller chloride doped in the crystal. As shown in Fig. S6, the diffraction intensity of PbI_2 and (100) plane is enhanced with the concentration of $Pb(SCN)_2$ additive increasing. Comprehensively, the optimal concentration of $Pb(SCN)_2$ additive is 2%. As presented in Fig. S7A, the optimal concentration of MACl solution is 3 mg/ml, as demonstrated by the highest diffraction intensity and the disappearance of the PbI_2 peak. Moreover, Fig. S7B illustrates that the (100) peak shifts to a higher degree as the concentration of MACl increases. This demonstrates that the compressive strain is formed on the surface owing to the smaller crystal lattice of $MAPbI_{3-x}Cl_x$ than WBG perovskite [45]. Based on these results, we speculate that chloride ions are incorporated into the crystal lattice to form GHJ. To further investigate this effect, we prepared samples containing 2% $Pb(SCN)_2$ additive and 3 mg/ml MACl. As presented in Fig. 3B, a distinct absorption onset is at around 750 nm in ultraviolet (UV)-visible (vis) absorption spectra. The absorption edge blue-shifted in the perovskite films with $Pb(SCN)_2$ additive and MACl posttreatment, indicating the presence of excessive PbI_2 and GHJ [39,46]. In addition, the absorbance is also enhanced owing to the improved crystallization after adding $Pb(SCN)_2$. Tauc curves were calculated using absorption spectra in Fig. S8. In comparison with the control sample, the optical bandgap of WBG films with excessive PbI_2 and GHJ enhanced from 1.686 to 1.696 and 1.698 eV, respectively. The steady-state photoluminescence (PL) spectra were measured using the samples prepared on an insulated substrate and covered by poly (methyl methacrylate) (PMMA). The control sample exhibits an emission peak located at around 749 nm, whereas the perovskite films with excessive PbI_2 and GHJ exhibit blue shift and enhanced intensity resulting from the suppression of nonradiative recombination [19,47]. Moreover, the PL spectra were measured from both the glass and PMMA sides to perform the difference between bulk and surface in Fig. S9. The perovskite films with GHJ exhibit a blue shift measured from the PMMA side, indicating that the GHJ is mainly located on the surface. The PL spectra were recorded after light soaking for 2 h in Fig. S10, where the sample with GHJ did not show halide segregation under continuous illumination in comparison with the control one. This demonstrates that the

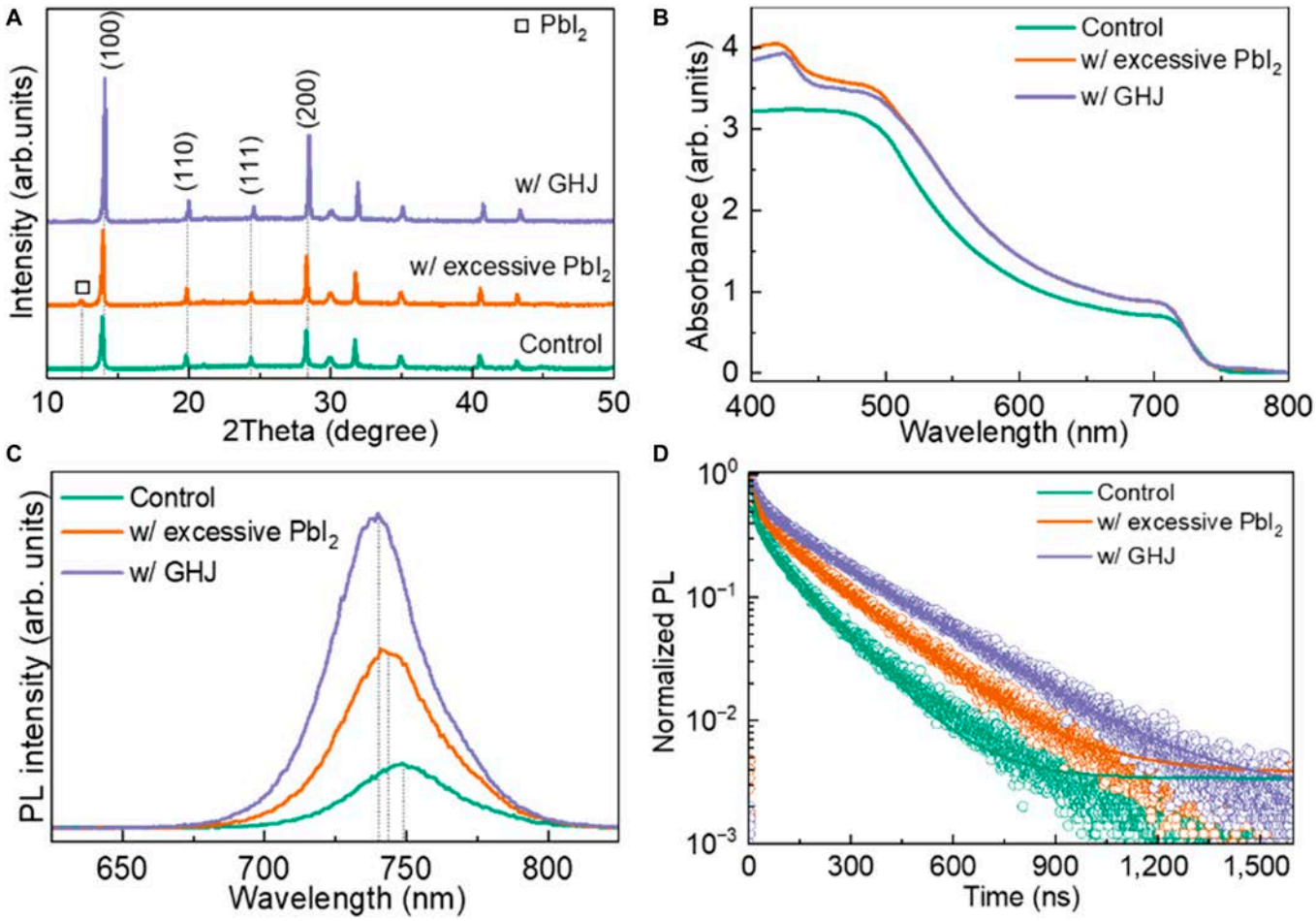


Fig. 3. (A) XRD patterns, (B) UV-vis absorption spectra, (C) PL spectra, and (D) TRPL curves of the control sample, and WBG films with excessive PbI_2 and GHJ, respectively.

compressive strain resulted in higher barrier of ion migration, suggesting that the GHJ can improve light stability and enhance operational stability [45,48]. Moreover, time-resolved photoluminescence (TRPL) is utilized to determine the carrier lifetime [26]. As presented in Fig. 3D and Table S1, the average lifetime was increased from 92.31 ns to 173.91 and 231.12 ns in the WBG films with excessive PbI_2 and GHJ, indicating enhanced carrier lifetime resulting from improved crystallization and passivated defects. Next, we further investigate the effect of GHJ on WBG films through electronic characterizations.

To investigate the surface variation, the contact potential difference (CPD) is determined by Kelvin probe force microscopy (KPFM). As presented in Fig. 4A and B, the CPD of perovskite film with GHJ is larger than the sample without GHJ, indicating a shift in the Fermi level upwards, which is beneficial for facilitating charge separation and carrier extraction [49–51]. In addition, the valence band and work function (W_f) are obtained by UV photoelectron spectroscopy [51,52]. As shown in Fig. 4C, the W_f is observed to decrease from 4.25 to 4.17 eV owing to the effect of GHJ, consisting well of the CPD change measured by KPFM. Furthermore, the valence band maximum (E_{VBM}) and conduction band minimum (E_{CBM}) were determined using the optical bandgap obtained from absorption. The energy level alignment is presented in Fig. 4D. An extra built-in electrical field is formed at GHJ to facilitate hole extraction and reduce charge recombination [34,53]. These results indicate that GHJ is beneficial for improving the electrical performance of WBG perovskite films.

We fabricated the PSCs with a configuration of ITO/SnO_2/WBG perovskite/Spiro-OMeTAD/Ag. Figure 5A presents the current density-voltage (*J-V*) curves of WBG PSCs without and with GHJ. The optimal WBG PSC with GHJ exhibited a high PCE of 20.30% with a V_{OC} of 1.185 V and fill factor (FF) of 0.805, whereas the control one displayed a low efficiency of 15.48% with a V_{OC} of 1.101 V and FF of 0.726, as shown in Table. Moreover, the short-circuit current density (J_{SC}) is also enhanced from 19.37 to 21.28 mA/cm^2. Additionally, the WBG PSC with GHJ demonstrated a lower hysteresis index than the one without GHJ (Fig. S11 and Table S2), indicating the suppression of defects and ions migration. As shown in Fig. 5B, the device with an area of 0.6 cm^2 displayed a PCE of 18.88%, which is slightly lower than the device with an area of 0.07 cm^2 of 19.89% (Table S3). The large-area device with 0.6 cm^2 further demonstrated the uniformity of GHJ on WBG perovskite films. To verify reproducibility, the photovoltaic parameters statistics of 20 independent devices are presented in Fig. S12. This also demonstrates the marked enhancement of V_{OC}, FF, and J_{SC} in the device with GHJ, resulting from improved crystallinity, passivated defects, and beneficial energy level alignment.

The external quantum efficiency (EQE) is presented in Fig. 5C, where the response of the PSC with GHJ is higher than the control one owing to its fast carrier extraction. Thus, the integrated current

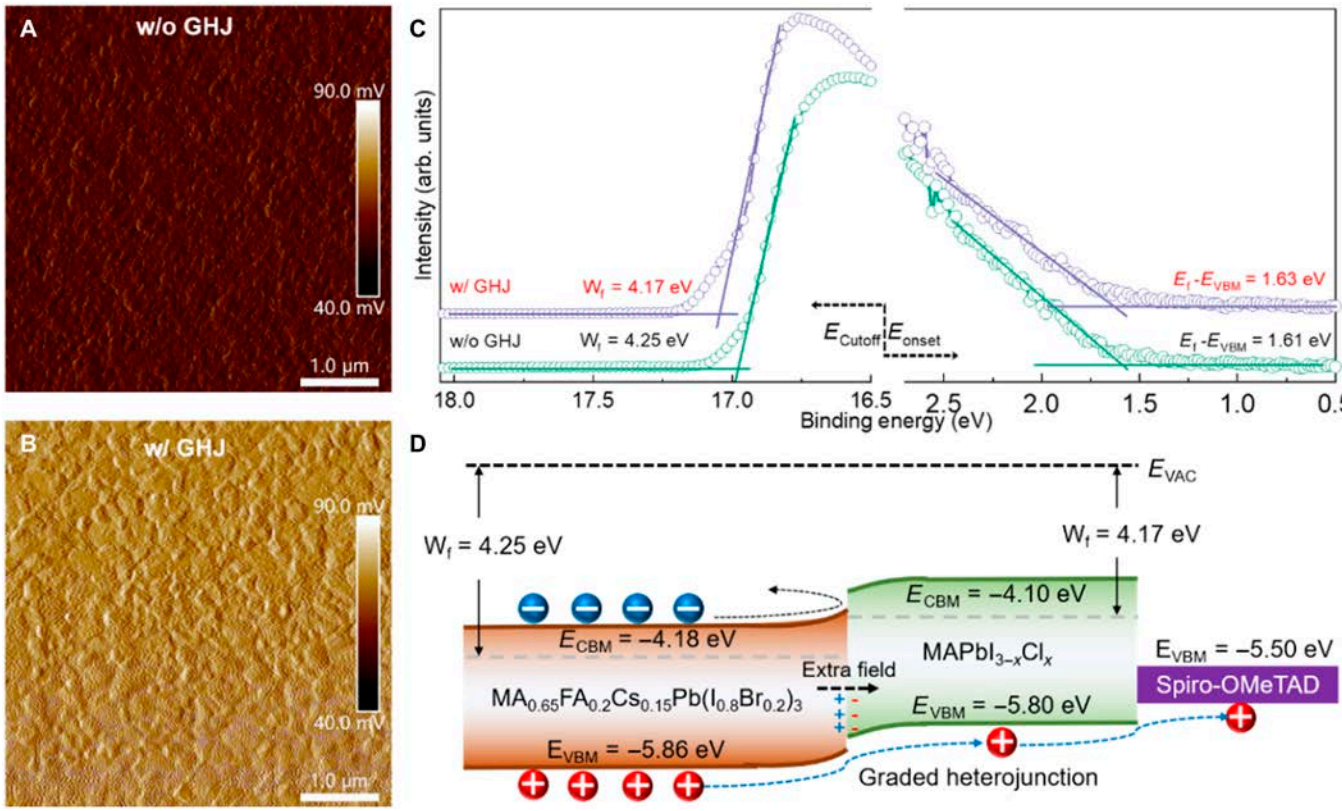


Fig. 4. KPFM images of WBG perovskite film (A) without and (B) with GHJ, respectively. (C) UV photoelectron spectroscopy spectra of WBG perovskite film without and with GHJ. (D) The schematic energy band diagrams of WBG perovskite film with GHJ.

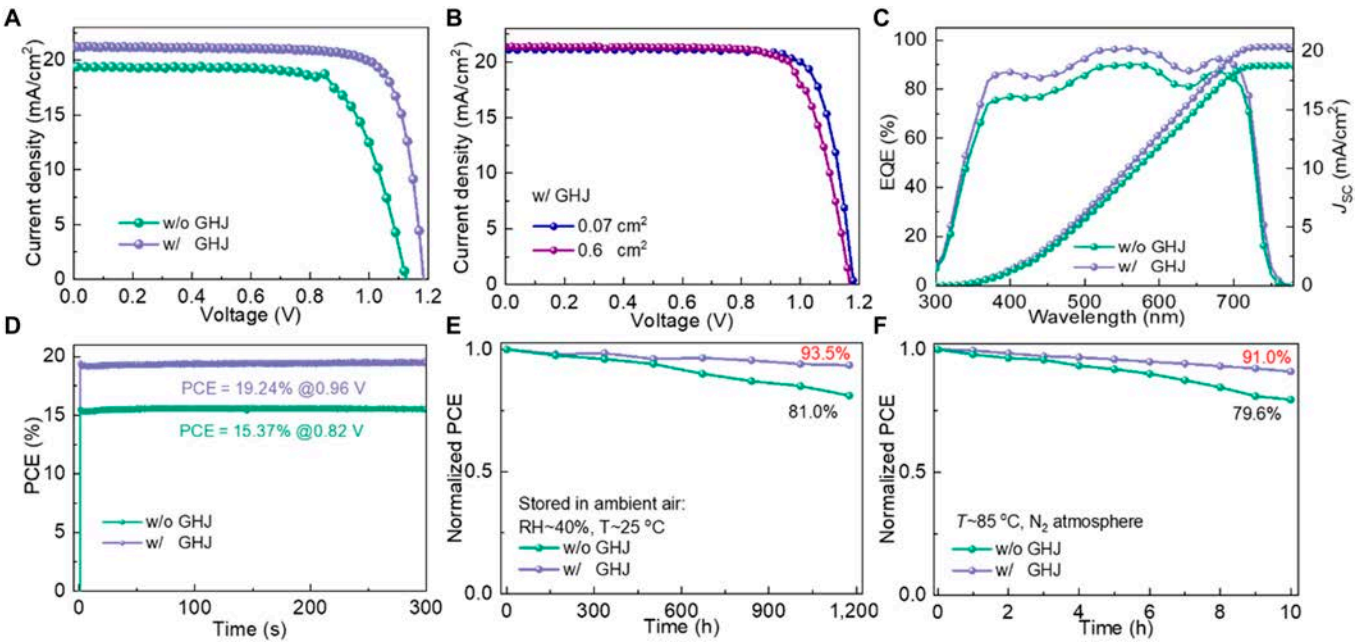


Fig. 5. (A) Light *J-V* curves of WBG PSCs without and with GHJ. (B) Light *J-V* curves of WBG PSCs with GHJ in active areas of 0.07 and 0.6 cm^2. (C) EQE spectra and integrated current of WBG PSCs without and with GHJ. (D) Steady output efficiency at MPP, (E) long-term storage stability in ambient, and (F) thermal stability at 85 °C of WBG PSCs without and with GHJ, respectively.

densities match well with the J_{SC} in *J-V* results. Meantime, the cutoff is approximately 750 nm, consisting well with the absorption. Additionally, the steady output efficiency was recorded at the maximum power point (MPP) for 300 s, as presented in Fig. 5D. The WBG PSC with GHJ displays a steady-output PCE of 19.24%, indicating its excellent operational stability. To further investigate

Table. Photovoltaic parameters for WBG PSCs without and with GHJ, respectively.

Samples	J_{SC} (mA/cm^2)	V_{OC} (V)	FF	PCE (%)
w/o GHJ	19.37	1.101	0.726	15.48
w/ GHJ	21.28	1.185	0.805	20.30

the illumination stability of the WBG PSCs, periodic photoresponses were measured in ambient air with a relative humidity (RH) of ~50%. The current was recorded under illumination with an on/off-modulated 405-nm laser, as shown in Fig. S13. The current remained almost undiminished for 19.5 h under alternating illumination and darkness conditions, indicating excellent operational stability exhibited in the WBG PSCs with GHJ in ambient air. The storage stability was tracked in ambient air with RH of approximately 40% and room temperature. As shown in Fig. 5E, the unencapsulated device with GHJ can maintain 93.5% of its initial efficiency after 1,200 hours of storage, but the control device only retained 81.0%. Moreover, the device with GHJ retained 91.0% of its initial efficiency after heating for 8 h, but the control sample decreased to 73.6%, as shown in Fig. 5F. This demonstrates that the GHJ is employed to improve the stability of WBG PSC owing to compressive strain on the surface. Overall, the WBG PSC with GHJ displays outstanding photovoltaic performance and stability in comparison with the control one.

To better understand the reason for GHJ on performance enhancement, several analyses were employed to examine the carrier dynamics. The space charge limited current is used to evaluate the trap-state density (n_t), which is proportional to the trap-filled limit voltage (V_{TFL}) [54,55]. As presented in Fig. S14, the V_{TFL} is decreased from 0.44 to 0.31 V, suggesting that defects are passivated in PSC with GHJ. The carrier-extraction and carrier-recombination lifetime was measured by transient photocurrent and transient photovoltage, respectively [56,57]. As shown in Fig. 6A and B, the WBG PSC with GHJ demonstrated a lower carrier-extraction lifetime (0.88 μs) than the control one (1.29 μs), indicating that the GHJ can facilitate carrier extraction at the interface. Meantime, the device with GHJ enhanced the carrier-recombination lifetime from 118 to 264 μs, suggesting that the defects on perovskite films are passivated. Moreover, Nyquist plots were obtained by ac impedance and fitted with an equivalent circuit (Fig. S15). As presented in Fig. 6C, the larger recombination resistance (1,775 Ω) exhibits in the device with GHJ than in the control one (1,522 Ω), resulting from the passivated defects on the surface [30]. In addition, the series resistance is reduced from 17 to 15 Ω owing to the improved crystallization, leading to the high J_{SC} of devices with

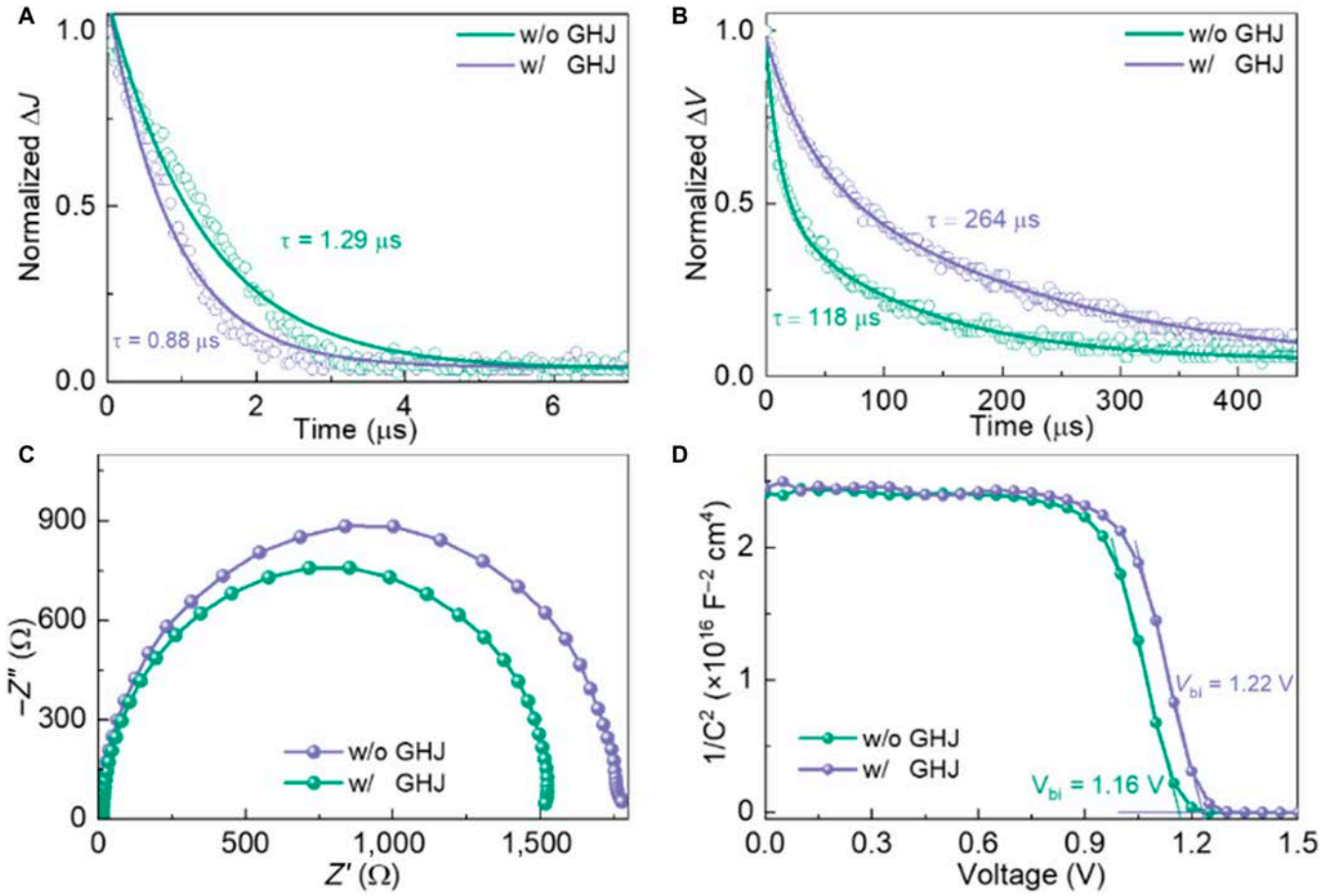


Fig. 6. (A) Transient photocurrent, (B) transient photovoltage, (C) Nyquist, and (D) Motto–Schottky curves of WBG PSCs without and with GHJ, respectively.

GHJ. Furthermore, the Motto–Schottky plots were used to estimate the built-in potential (V_{bi}) by capacitance-voltage (*C-V*) measurement [42]. As demonstrated in Fig. 6D, the V_{bi} was increased from 1.16 to 1.22 V because of the suppressed nonradiative recombination and improved energy level alignment. The larger V_{bi} is conducive to increasing the force of carrier extraction and stretching depletion region, further enhancing the V_{OC} of PSC [28,58].

The 4-T tandem solar cells were fabricated by combining semitransparent WBG PSCs with TOPCon silicon solar cells, as presented in Fig. 7A. A thin layer of molybdenum oxide (MoO_x) was deposited on Spiro-OMeTAD to protect it during the preparation of the indium-zinc-oxide transparent electrode by sputtering. The *J-V* curves were independently measured for semitransparent WBG PSC and TOPCon silicon solar cells. As presented in Fig. 7B and Table S4, the semitransparent WBG PSC exhibited an efficiency of 20.13%. In addition, the TOPCon silicon solar cell displayed a PCE of 22.50%, which decreased to 10.78% after filtering with semitransparent WBG PSC. As shown in Fig. S16, a semitransparent WBG device with an area of 4.5 × 4.5 cm^2 was used as a filter during to test silicon solar cells. Consequently, the 4-T tandem device eventually achieved a recorded PCE of 30.91%. Figure 7C and Table S5 summarize the state-of-the-art efficiencies of 4-T perovskite-silicon tandem solar cells, which indicate obviously that the PCE achieved herein represents the highest level among them. To demonstrate the reliability of *J-V* results, we also measured the EQE response of the semitransparent WBG PSC, as depicted in Fig. S17. The integrated current is 20.68 mA/cm^2, close to the J_{SC} acquired in the *J-V* results. Now, the operational lifetime of silicon solar cells is up to 25 years. Thus, the reliability of the tandem device depends on the perovskite material. As demonstrated in Fig. 7D, the efficiency of semitransparent WBG PSC remained at 18.55% after storage for 1,000 h in ambient air with an RH of 40%. The compact indium-zinc-oxide electrode effectively prevented humidity erosion, and the perovskite film was improved by GHJ, resulting in excellent stability of the semitransparent solar cells. These outstanding results suggest that GHJ has the potential to improve WBG PSCs while also enabling the development of highly efficient and stable perovskite/silicon tandem solar cells.

Discussion

In summary, we employed the conventional additive of $Pb(SCN)_2$ and MACl posttreatment to construct GHJ on the surface of WBG PSCs. The $Pb(SCN)_2$ additive improved crystallinity, and formed excessive PbI_2, while MACl reacted with excessive PbI_2 and transformed it into $MAPbI_{3-x}Cl_x$ perovskite. This results in the formation of GHJ and compressive strain, which were

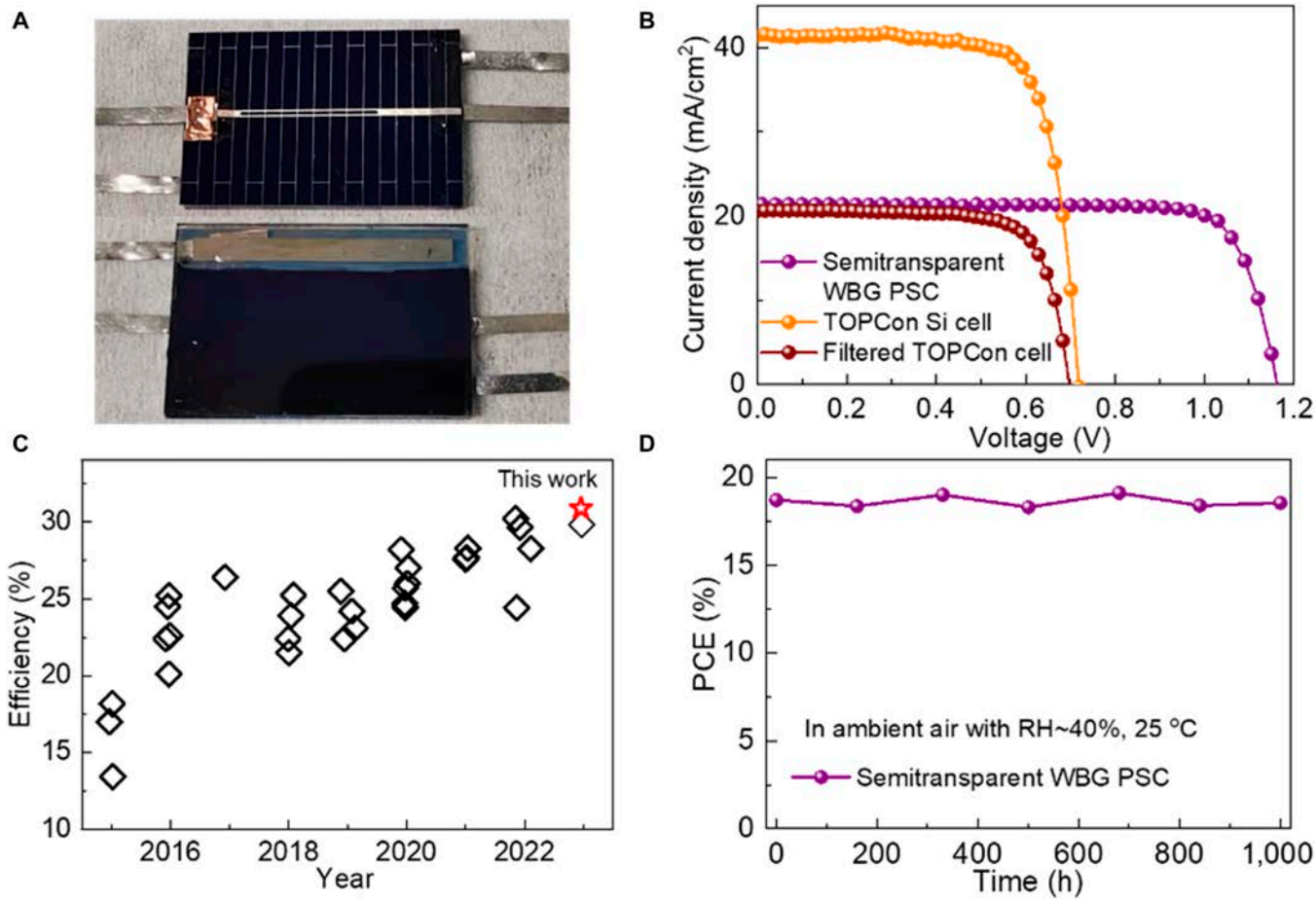


Fig. 7. (A) Photograph of the fabricated 4-T WBG perovskite/TOPCon silicon tandem device. (B) *J-V* curves of semitransparent WBG PSC as well as TOPCon silicon solar cells before and after filtering with the semitransparent device. (C) Summary of the state-of-the-art efficiencies of 4-T perovskite-silicon tandem solar cells. (D) PCE variation of semitransparent WBG PSC after storage in ambient air.

beneficial in passivating defects, suppressing ion migration, and facilitating carrier extraction. Consequently, the WBG PSC with GHJ achieved a remarkable PCE of 20.30%, with a high V_{OC} of 1.185 V, and retained 93.5% of the initial value after storage in ambient air with an RH of 40% for 1,200 h. Moreover, the 4-T WBG perovskite/TOPCon silicon tandem device shows a recorded efficiency of 30.91% and excellent stability. These findings have important implications for the fabrication of highly efficient and stable perovskite/silicon tandem solar cells.

Materials and Methods

The materials and methods can be found in the Supplementary Materials.

Acknowledgments

Funding: The authors gratefully acknowledge the financial support from the National Key R&D Program of China (2022YFB3605402, 2021YFF0500501), the Fundamental Research Funds for the Central Universities (YJSJ23019), the National Natural Science Foundation of China (62274132, 61804113, 61874083, and 62204189), Young Talent Fund of Association for Science and Technology in Shaanxi (20220115), and the Natural Science Basic Research Program of Shaanxi (2021JC-24). **Author contributions:** W.C. and L.L. fabricated and characterized perovskite films and devices. W.C. wrote the draft of the manuscript. W.Z. and C.Z. designed and supervised the research. All authors contributed to the discussion and commented on the manuscript. **Competing interests:** The authors declare that there are no conflicts of interest regarding the publication of this article.

Data Availability

All data are available in the main text or the Supplementary Materials.

Supplementary Materials

Materials and Methods.
Fig. S1. XPS core-level spectra for S 2p of control WBG perovskite film, the samples with $Pb(SCN)_2$ additive, and MACl post-treatment.
Fig. S2. (A) XPS spectra of WBG perovskite film with GHJ after etching with 0, 30, and 60 s. Core-level (B) Cl 2p, (C) Pb 4f, and (D) I 3d XPS spectra of WBG perovskite film with GHJ after etching with 0, 30, and 60 s, respectively.
Fig. S3. The statistical grain size of (A) control sample as well as WBG films with (B) excessive PbI_2 and (C) GHJ, respectively.
Fig. S4. SEM images of WBG films with excessive PbI_2 (A) before and (B) after IPA washing, respectively.
Fig. S5. Magnified (100) and (200) XRD peaks of the control sample as well as WBG films with excessive PbI_2 and GHJ, respectively.
Fig. S6. XRD patterns of control sample as well as WBG films with 1%, 2%, 3% $Pb(SCN)_2$ additive.
Fig. S7. (A) XRD patterns and (B) magnified (100) XRD peak of WBG films with 2% $Pb(SCN)_2$ additive after treating with 0, 1, 3, and 5 mg/mL MACl/IPA solution.
Fig. S8. Tauc curves of (A) control sample as well as WBG films with (B) excessive PbI_2 and (C) GHJ, respectively.
Fig. S9. PL spectra measured from PMMA and glass sides, respectively.
Fig. S10. PL spectra of WBG films (A) without and (B) with GHJ measured after light soaking for 0, 1, and 2 h, respectively.
Fig. S11. *J-V* curves measured by forward and reverse scanning, respectively.
Fig. S12. Statistical (A) V_{OC}, (B) FF, (C) JSC, and (D) PCE of 20 independent WBG PSCs without and with GHJ, respectively.
Fig. S13. Response properties evaluated with an on/off-modulated 405 nm laser (40 mW cm^{-2}) for the typical WBG PSC with GHJ recorded in ambient air.
Fig. S14. SCLC curves of WBG films (A) without and (B) with GHJ, respectively.
Fig. S15. Equivalent circuit model for fitting the Nyquist plots.
Fig. S16. Photograph of large-area semitransparent WBG device used as a filter.
Fig. S17. EQE and integrated current of semitransparent WBG PSC.
Table S1. Fitting parameters for the TRPL decay of the control sample as well as WBG films with excessive PbI_2 and GHJ, respectively.
Table S2. Photovoltaic parameters for WBG PSCs without and with GHJ measured by forward and reverse scanning, respectively.
Table S3. Photovoltaic parameters for WBG PSCs with GHJ in an area of 0.07 and 0.6 cm^2.
Table S4. Photovoltaic parameters for semitransparent WBG PSC as well as TOPCon silicon solar cells before and after filtering with the semitransparent device.
Table S5. A summary of the state-of-the-art efficiencies of semi-transparent PSCs and 4-T perovskite/silicon tandem devices.

References

1. Correa-Baena J-P, Saliba M, Buonassisi T, Grätzel M, Abate A, Tress W, Hagfeldt A. Promises and challenges of perovskite solar cells. *Science*. 2017;358(6364):739–744.
2. De Wolf S, Holovsky J, Moon S-J, Loper P, Niesen B, Ledinsky M, Haug F-J, Yum J-H, Ballif C. Organometallic halide perovskites: Sharp optical absorption edge and its relation to photovoltaic performance. *J Phys Chem Lett*. 2014;5(6):1035–1039.
3. Green MA, Ho-Baillie A, Snaith HJ. The emergence of perovskite solar cells. *Nat Phot*. 2014;8(7):506–514.
4. Park N-G. Perovskite solar cells: An emerging photovoltaic technology. *Mater Today*. 2015;18(2):65–72.
5. Rong Y, Hu Y, Mei A, Tan H, Saidaminov MI, Seok SI, McGehee MD, Sargent EH, Han H. Challenges for commercializing perovskite solar cells. *Science*. 2018;361(6408):Article eaat8235.
6. Yin WJ, Shi T, Yan Y. Unique properties of halide perovskites as possible origins of the superior solar cell performance. *Adv Mater*. 2014;26(27):4653–4658.
7. NRE Laboratory, Best Research Cell Efficiency Chart. 2023. [accessed 1 Jun 2023] https://www.nrel.gov/pv/cell-efficiency.html
8. Park J, Kim J, Yun H-S, Paik MJ, Noh E, Mun HJ, Kim MG, Shin TJ, Seok SI. Controlled growth of perovskite layers with volatile alkylammonium chlorides. *Nature*. 2023;616(7958):724–730.
9. Al-Ashouri A, Köhnen E, Li B, Magomedov A, Hempel H, Caprioglio P, Márquez JA, Morales Vilches AB, Kasparavicius E,

Smith JA. Monolithic perovskite/silicon tandem solar cell with> 29% efficiency by enhanced hole extraction. *Science*. 2020;370(6522):1300–1309.
10. Wang Z, Zhu X, Zuo S, Chen M, Zhang C, Wang C, Ren X, Yang Z, Liu Z, Xu X, et al. 27%-efficiency four-terminal perovskite/silicon tandem solar cells by sandwiched gold nanomesh. *Adv Funct Mater*. 2020;30(4):Article 1908298.
11. Yang D, Zhang X, Hou Y, Wang K, Ye T, Yoon J, Wu C, Sanghadasa M, Liu SF, Priya S. 28.3%-efficiency perovskite/silicon tandem solar cell by optimal transparent electrode for high efficient semitransparent top cell. *Nano Energy*. 2021;84:Article 105934.
12. Yu ZJ, Leilaeioun M, Holman Z. Selecting tandem partners for silicon solar cells. *Nat Energy*. 2016;1(11):1–4.
13. Fang Z, Zeng Q, Zuo C, Zhang L, Xiao H, Cheng M, Hao F, Bao Q, Zhang L, Yuan Y. Perovskite-based tandem solar cells. *Sci Bull*. 2021;66(6):621–636.
14. Li H, Zhang W. Perovskite tandem solar cells: From fundamentals to commercial deployment. *Chem Rev*. 2020;120(18):9835–9950.
15. Zhao D, Wang C, Song Z, Yu Y, Chen C, Zhao X, Zhu K, Yan Y. Four-terminal all-perovskite tandem solar cells achieving power conversion efficiencies exceeding 23%. *ACS Energy Lett*. 2018;3(2):305–306.
16. Tao L, Qiu J, Sun B, Wang X, Ran X, Song L, Shi W, Zhong Q, Li P, Zhang H, et al. Stability of mixed-halide wide bandgap perovskite solar cells: Strategies and progress. *J Energy Chem*. 2021;61:395–415.
17. Jaysankar M, Raul BA, Bastos J, Burgess C, Weijtens C, Creatore M, Aernouts T, Kuang Y, Gehlhaar R, Hadipour A. Minimizing voltage loss in wide-bandgap perovskites for tandem solar cells. *ACS Energy Lett*. 2018;4(1):259–264.
18. Xu J, Boyd CC, Yu ZJ, Palmstrom AF, Witter DJ, Larson BW, France RM, Werner J, Harvey SP, Wolf EJ, et al. Triple-halide wide–band gap perovskites with suppressed phase segregation for efficient tandems. *Science*. 2020;367(6482):1097–1104.
19. Yang G, Ni Z, Yu ZJ, Larson BW, Yu Z, Chen B, Alasfour A, Xiao X, Luther JM, Holman ZC, et al. Defect engineering in wide-bandgap perovskites for efficient perovskite–silicon tandem solar cells. *Nat Phot*. 2022;16(8):588–594.
20. Yao Y, Hang P, Li B, Hu Z, Kan C, Xie J, Wang Y, Zhang Y, Yang D, Yu X. Phase-stable wide-bandgap perovskites for four-terminal perovskite/silicon tandem solar cells with over 30% efficiency. *Small*. 2022;18(38):Article 2203319.
21. Emshadi K, Ghimire N, Gurung A, Bahrami B, Pathak R, Bobba RS, Lamsal BS, Rahman SI, Chowdhury AH, Chen K, et al. Tailoring the grain boundaries of wide-bandgap perovskite solar cells by molecular engineering. *Sol RRL*. 2020;4(12):Article 2000384.
22. Liang J, Chen C, Hu X, Xiao M, Wang C, Yao F, Li J, Wang H, He J, Da B. Revealing the mechanism of π aromatic molecule as an effective Passivator and stabilizer in highly efficient wide-bandgap perovskite solar cells. *Sol. RRL*. 2021;5(8):Article 2100249.
23. Khadka DB, Shirai Y, Yanagida M, Noda T, Miyano K. Tailoring the open-circuit voltage deficit of wide-band-gap perovskite solar cells using alkyl chain-substituted fullerene derivatives. *ACS Appl Mater Interfaces*. 2018;10(26):22074–22082.
24. Lin Y, Chen B, Zhao F, Zheng X, Deng Y, Shao Y, Fang Y, Bai Y, Wang C, Huang J. Matching charge extraction contact for wide-bandgap perovskite solar cells. *Adv Mater*. 2017;29(26):Article 1700607.
25. Liu L, Yang Y, Du M, Cao Y, Ren X, Zhang L, Wang H, Zhao S, Wang K, Liu S. Self-assembled amphiphilic monolayer for efficient and stable wide-bandgap perovskite solar cells. *Adv Energy Mater*. 2023;13(4):Article 2202802.
26. Chen C, Liang J, Zhang J, Liu X, Yin X, Cui H, Wang H, Wang C, Li Z, Gong J, et al. Interfacial engineering of a thiophene-based 2D/3D perovskite heterojunction for efficient and stable inverted wide-bandgap perovskite solar cells. *Nano Energy*. 2021;90:Article 106608.
27. Kim D, Jung HJ, Park IJ, Larson BW, Dunfield SP, Xiao C, Kim J, Tong J, Boonmongkolras P, Ji SG, et al. Efficient, stable silicon tandem cells enabled by anion-engineered wide-bandgap perovskites. *Science*. 2020;368(6487):155–160.
28. Pham H, Yin Y, Peng J, Mahmud MA, Wu Y, Shen H, Zheng J, Tran-Phu T, Lu T, Li L. Efficient and stable wide bandgap perovskite solar cells through surface passivation with long alkyl chain organic cations. *J Mater Chem A*. 2021;9(34):18454–18465.
29. Gharibzadeh S, Abdollahi Nejand B, Jakoby M, Abzieher T, Hauschild D, Moghadamzadeh S, Schwenzer JA, Brenner P, Schmager R, Haghighirad AA, et al. Record open-circuit voltage wide-bandgap perovskite solar cells utilizing 2D/3D perovskite heterostructure. *Adv Energy Mater*. 2019;9(21):Article 1803699.
30. Yu Y, Liu R, Liu C, Shi XL, Yu H, Chen ZG. Synergetic regulation of oriented crystallization and interfacial passivation enables 19.1% efficient wide-bandgap perovskite solar cells. *Adv Energy Mater*. 2022;12(33):2201509.
31. Chen Y, Sun Y, Peng J, Tang J, Zheng K, Liang Z. 2D Ruddlesden–Popper perovskites for optoelectronics. *Adv Mater*. 2018;30(2):Article 1703487.
32. Mahmud MA, Duong T, Yin Y, Pham HT, Walter D, Peng J, Wu Y, Li L, Shen H, Wu N, et al. Double-sided surface passivation of 3D perovskite film for high-efficiency mixed-dimensional perovskite solar cells. *Adv Funct Mater*. 2020;30(7):Article 1907962.
33. Nie T, Fang Z, Ren X, Duan Y, Liu S. Recent advances in wide-bandgap organic–inorganic halide perovskite solar cells and tandem application. *Nano-Micro Lett*. 2023;15(1):Article 70.
34. Chen C, Song Z, Xiao C, Zhao D, Shrestha N, Li C, Yang G, Yao F, Zheng X, Ellingson RJ, et al. Achieving a high open-circuit voltage in inverted wide-bandgap perovskite solar cells with a graded perovskite homojunction. *Nano Energy*. 2019;61:141–147.
35. Bi C, Yuan Y, Fang Y, Huang J. Low-temperature fabrication of efficient wide-bandgap organolead trihalide perovskite solar cells. *Adv Energy Mater*. 2015;5(6):Article 1401616.
36. Kim DH, Muzzillo CP, Tong J, Palmstrom AF, Larson BW, Choi C, Harvey SP, Glynn S, Whitaker JB, Zhang F, et al. Bimolecular additives improve wide-band-gap perovskites for efficient tandem solar cells with CIGS. *Joule*. 2019;3(7):1734–1745.
37. Huang Y, Wu S, Chen R, Fang S, Zhang S, Wang G, Chen W. Efficient methylamine-containing antisolvent strategy to fabricate high-efficiency and stable $FA_{0.85}Cs_{0.15}P(Br_{0.15}I_{2.85})$ perovskite solar cells. *ACS Appl Mater Interfaces*. 2019;11(20):18415–18422.
38. Yu Y, Wang C, Grice CR, Shrestha N, Chen J, Zhao D, Liao W, Cimaroli AJ, Roland PJ, Ellingson RJ, et al. Improving the performance of formamidinium and cesium lead triiodide perovskite solar cells using lead thiocyanate additives. *ChemSusChem*. 2016;9(23):3288–3297.
39. Yu Y, Wang C, Grice CR, Shrestha N, Zhao D, Liao W, Guan L, Awni RA, Meng W, Cimaroli AJ, et al. Synergistic effects of lead thiocyanate additive and solvent annealing on the

performance of wide-bandgap perovskite solar cells. *ACS Energy Lett*. 2017;2(5):1177–1182.
40. Kim MK, Jeon T, Park HI, Lee JM, Nam SA, Kim SO. Effective control of crystal grain size in CH 3 NH 3 PbI 3 perovskite solar cells with a pseudohalide $Pb(SCN)_2$ additive. *CrystEngComm*. 2016;18(32):6090–6095.
41. Li X, Du J, Duan H, Wang H, Fan L, Sun Y, Sui Y, Yang J, Wang F, Yang L. Moisture-preventing $MAPbI_3$ solar cells with high photovoltaic performance via multiple ligand engineering. *Nano Res*. 2022;15(2):1375–1382.
42. Chai W, Zhu W, Zhang Z, Xi H, Chen D, Zhu J, Zhang J, Zhang C, Hao Y. Selectively localized growth of two-dimensional perovskites at grain boundaries for efficient and stable $CsPbI_3$ perovskite solar cells. *Mater Today Phys*. 2023;34:Article 101088.
43. Zhu X, Yang S, Cao Y, Duan L, Du M, Feng J, Jiao Y, Jiang X, Sun Y, Wang H. Ionic-liquid-perovskite capping layer for stable 24.33%-efficient solar cell. *Adv Energy Mater*. 2022;12(6):Article 2103491.
44. Yao Z, Jin Z, Zhang X, Wang Q, Zhang H, Xu Z, Ding L, Liu SF. Pseudohalide (SCN^-)-doped $CsPbI_3$ for high-performance solar cells. *J Mater Chem C*. 2019;7(44):13736–13742.
45. Hang P, Kan C, Li B, Yao Y, Hu Z, Zhang Y, Xie J, Wang Y, Yang D, Yu X. Highly efficient and stable wide-bandgap perovskite solar cells via strain management. *Adv Funct Mater*. 2023;33(11):Article 2214381.
46. Yang Z, Rajagopal A, Jo SB, Chueh C-C, Williams S, Huang C-C, Katahara JK, Hillhouse HW, Jen AK-Y. Stabilized wide bandgap perovskite solar cells by tin substitution. *Nano Lett*. 2016;16(12):7739–7747.
47. Hu M, Bi C, Yuan Y, Bai Y, Huang J. Stabilized wide bandgap $MAPbBr_xI_{3-x}$ perovskite by enhanced grain size and improved crystallinity. *Adv Sci*. 2016;3(6):Article 1500301.
48. Xue D-J, Hou Y, Liu S-C, Wei M, Chen B, Huang Z, Li Z, Sun B, Proppe AH, Dong Y, et al. Regulating strain in perovskite thin films through charge-transport layers. *Nat Commun*. 2020;11(1):Article 1514.
49. Li Z, Kim TH, Han SY, Yun YJ, Jeong S, Jo B, Ok SA, Yim W, Lee SH, Kim K, et al. Wide-bandgap perovskite/gallium arsenide tandem solar cells. *Adv Energy Mater*. 2020;10(6):Article 1903085.
50. Saidaminov MI, Williams K, Wei M, Johnston A, Quintero-Bermudez R, Vafaie M, Pina JM, Proppe AH, Hou Y, Walters G, et al. Multi-cation perovskites prevent carrier reflection from grain surfaces. *Nat Mater*. 2020;19(4):412–418.
51. Liu Z, Chang J, Lin Z, Zhou L, Yang Z, Chen D, Zhang C, Liu S, Hao Y. High-performance planar perovskite solar cells using low temperature, solution–combustion-based nickel oxide hole transporting layer with efficiency exceeding 20%. *Adv Energy Mater*. 2018;8(19):Article 1703432.
52. Li Y, Wu J, Zhang Y, Zhang L, Zhou X, Hu B, Jiang Z, Zeng J, Wang D, Liu Y, et al. Whether organic spacer cations induced 2D/3D or quasi-2D/3D mixed dimensional perovskites? *Chem Eng J*. 2022;450:Article 137887.
53. Han D, Yuan Q, Slanina Z, Tang X, Yi S, Zhou D-Y, Uhlik F, Feng L. Enhancing built-in electric field and defect passivation through gradient doping in inverted $CsPbI_2Br$ perovskite solar cells. *Sol. RRL*. 2021;5(1):Article 2000629.
54. Huo X, Li Y, Liu W, Huang X, Meng J, Lu Y, Meng N, Zhang Y, Zhao S, Qiao B, et al. Nonpolar and ultra-long-chain ligand to modify the perovskite Interface toward high-efficiency and stable wide bandgap perovskite solar cells. *ACS Appl Energy Mater*. 2023;6(3):1731–1740.
55. Wang D, Li W, Sun W, Liu X, Li G, Wu Z, Wu J, Lan Z. Guanidinium iodide modification enabled highly efficient and stable all-inorganic $CsPbBr_3$ perovskite solar cells. *Electrochim Acta*. 2021;365:Article 137360.
56. Zhou L, Chang J, Liu Z, Sun X, Lin Z, Chen D, Zhang C, Zhang J, Hao Y. Enhanced planar perovskite solar cell efficiency and stability using a perovskite/PCBM heterojunction formed in one step. *Nanoscale*. 2018;10(6):3053–3059.
57. Huang X, Bi W, Jia P, Tang Y, Lou Z, Hu Y, Cui Q, Hou Y, Teng F. Enhanced efficiency and light stability of planar perovskite solar cells by diethylammonium bromide induced large-grain 2D/3D hybrid film. *Org Electron*. 2019;67:101–108.
58. Hu X, Jiang XF, Xing X, Nian L, Liu X, Huang R, Wang K, Yip HL, Zhou G. Wide-bandgap perovskite solar cells with large open-circuit voltage of 1653 mV through interfacial engineering. *Sol. RRL*. 2018;2(8):Article 1800083.